Transient Stress-Coupling Between the 1992 Landers and 1999 Hector Mine, California, Earthquakes

by Timothy Masterlark and Herbert F. Wang

Abstract   A three-dimensional finite-element model (FEM) of the Mojave block region in southern California is constructed to investigate transient stress-coupling between the 1992 Landers and 1999 Hector Mine earthquakes. The FEM simulates a poroelastic upper-crust layer coupled to a viscoelastic lower-crust layer, which is decoupled from the upper mantle. FEM predictions of the transient mechanical behavior of the crust are constrained by global positioning system (GPS) data, interferometric synthetic aperture radar (InSAR) images, fluid-pressure data from water wells, and the dislocation source of the 1999 Hector Mine earthquake. Two time-dependent parameters, hydraulic diffusivity of the upper crust and viscosity of the lower crust, are calibrated to 10^{-2} m^2·sec^{-1} and 5×10^{18} Pa·sec respectively. The hydraulic diffusivity is relatively insensitive to heterogeneous fault-zone permeability specifications and fluid-flow boundary conditions along the elastic free-surface at the top of the problem domain. The calibrated FEM is used to predict the evolution of Coulomb stress during the interval separating the 1992 Landers and 1999 Hector Mine earthquakes. The predicted change in Coulomb stress near the hypocenter of the Hector Mine earthquake increases from 0.02 to 0.05 MPa during the 7-yr interval separating the two events. This increase is primarily attributed to the recovery of decreased excess fluid pressure from the 1992 Landers coseismic (undrained) strain field. Coulomb stress predictions are insensitive to small variations of fault-plane dip and hypocentral depth estimations of the Hector Mine rupture.

Introduction

During the 1990s, two large seismic events (the 28 June 1992 M_w 7.3 Landers and 16 October 1999 M_w 7.1 Hector Mine earthquakes) occurred in the Mojave block of southern California. The abundance of deformational data associated with the 1992 Landers earthquake provides unprecedented opportunities to characterize transient, postseismic surface deformation. Several mechanisms have been proposed to explain postseismic deformation, including gravity loading, afterslip, viscoelastic relaxation, and poroelastic effects. Gravity loading causes transient deformation due to the equilibration of coseismic vertical deformation. Although the effects of gravity loading occur over a regional scale (Pollitz, 1997), the expected magnitude of deformation is much less than that of the other postseismic deformation mechanisms, and gravity-loading effects are neglected in this study. Models with a single deformational mechanism are insufficient to explain observations (e.g., Savage and Svarc, 1997; Deng et al., 1998). A combination of deformational mechanisms is necessary to account for observed deformation, and it has been recognized that poroelastic effects must be accounted for in models of postseismic deformation for the 1992 Landers earthquake (Peltzer et al., 1996,

1998; Bosl and Nur, 1998). Poroelastic theory predicts strain from seismic displacement will produce significant excess fluid pressure in the near-field region. Likewise, the decay of this excess fluid pressure will induce transient deformation. Although afterslip may contribute significantly to postseismic deformation, we assume that shear stress relaxation in the lower crust is entirely due to viscoelastic relaxation. Furthermore, for the case of strike-slip dislocation, surface deformation derived from the two mechanisms is indistinguishable (Savage, 1990). We investigate transient postseismic deformation associated with fluid flow and viscoelastic relaxation due to the Landers earthquake and quantify the quasistatic coupling between the 1992 Landers and 1999 Hector Mine earthquakes.

Recent Mojave Block Earthquakes

The Mojave block is a wedge-shaped structure bound to the west by the San Andreas fault (SAF) and to the north by the Garlock fault (Fig. 1). The eastern edge of the block is marked by north-trending geophysical, crust thickness, and physiography discontinuities (Dokka, 1980). The east-

Epicenters

① Landers, M_W = 7.3
6/28/1992, (t = 0)

② Big Bear, M_W = 6.1
6/28/1992, (t = 188 min.)

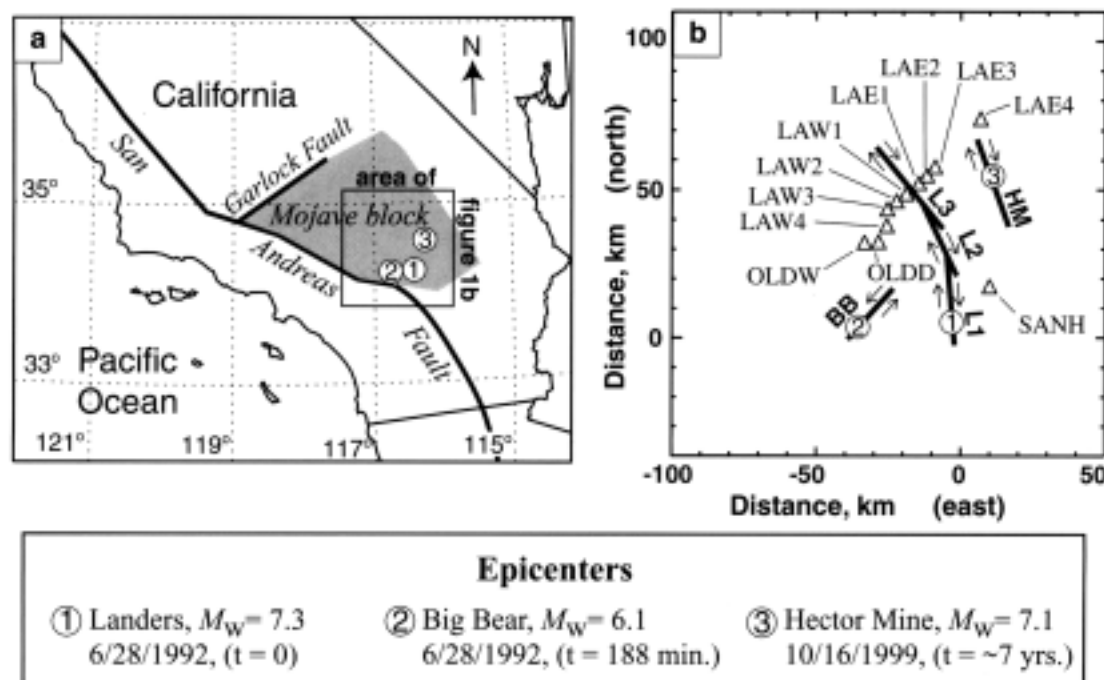③ Hector Mine, M_W = 7.1
10/16/1999, (t = ~7 yrs.)

Figure 1. Map of study area. (a) The Mojave block (shaded region) of southern California. (b) Site location, 1992 Landers, California earthquake. The fault trace is simplified to include three fault segments: L1, L2, and L3. Left-lateral rupture along the Big Bear (BB) fault occurred 188 minutes after the Landers rupture. A single 23-km fault striking northeast with an epicenter located 7 km from the southwest end is assumed. The Hector Mine epicenter is located 30 km northeast of the Landers rupture. The simplified rupture plane is labeled HM. Labeled triangles mark the locations of the 11 GPS stations used for calibration of the transient model.

ern edge of the Mojave block appears to mark the western boundary of the rigid North American plate (Bennett *et al.*, 1999). The Mojave block is cut by several northwest-trending faults with right-lateral offsets. Slip rates for the individual faults are relatively small (less than 1.0 mm·yr^{-1}) (Hauksson *et al.*, 1993). The Mojave block is part of the eastern California shear zone, an 80-km-wide region that extends northwest from the southeast corner of California through the Death Valley region and that may accommodate as much as 29% of the total plate motion between the North American and Pacific plates (Miller *et al.*, 2001).

Rupture from the 28 June 1992 Landers, California, earthquake occurred along five major and several minor fault segments within the Mojave block. The hypocentral depth was about 8 km (Qu *et al.*, 1994). The dislocation was primarily right-lateral strike slip, with up to 6 m of offset observed along the 85-km surface trace of the rupture (Wald and Heaton, 1994) (Fig. 1b). A wide variety of quantitative data, including strain meter, water level, very long baseline interferometry (VLBI), GPS, and InSAR images were collected, in part due to the event's location in the desert and relatively large magnitude.

The M_w 6.1 Big Bear earthquake occurred about three hours after the Landers earthquake. Rupture from this earthquake did not reach the surface. Initial investigations of focal

mechanisms and aftershock data (Hauksson *et al.*, 1993) suggested left-lateral slip along a northeast trending fault plane. Others have suggested a more complex rupture pattern, which may include multiple smaller events along both conjugate planes with a focal depth of 11–14 km (Jones and Hough, 1995).

The 16 October 1999 M_w 7.1 Hector Mine, California, earthquake ruptured the Lavic Lake fault and a series of northwest-trending faults that are subparallel to the rupture of the 1992 Landers earthquake. The focal mechanism of the Hector Mine earthquake mainshock includes a nodal plane trending north-northwest and dipping 77° (Parsons and Dreger, 2000) and a hypocentral depth of about 5 km (Dreger and Kaverina, 2000; Parsons and Dreger, 2000; Scientists of the USGS *et al.*, 2000). The fault trace is about 30 km east of the 1992 Landers rupture. Slip is primarily right lateral, with an average magnitude of 3 m. Ground-based measurements indicate a maximum dislocation of 5.25 m (Scientists of the USGS *et al.*, 2000), while InSAR images suggest a maximum slip of 7 m (Sandwell *et al.*, 2000). We assume rupture along a single fault plane for the 1999 Hector Mine earthquake (Hurst *et al.*, 2000), because we consider the deformation leading to, but not including, the initiation of the Hector Mine rupture.

Initial investigations of static coupling between the

1992 Landers and 1999 Hector Mine earthquakes are some-what inconclusive (Wyss and Wiemer, 2000; Harris and Simpson, 2002). Some studies report that the hypocenter of the 1999 Hector Mine earthquake is in the stress shadow of the 1992 Landers earthquake (e.g., Hauksson et al., 1999; Wyss et al., 1999), while others suggest the opposite (Parsons and Dreger, 2000). These static-coupling analyses utilize simplified fluid-pressure treatments and neglect transient effects. Furthermore, the analyses include homogeneous elastic half-space (HEHS) models, which may be poor representations of the real mechanical system. In this study, we will demonstrate that significant changes in stress and fluid pressure evolved over the 7-yr interval that separates the two events.

Finite-Element Model

The finite-element code ABAQUS (Hibbit, Karlsson & Sorensen, Inc., 1998) is used to solve the governing equations for displacement in a linear (Maxwell) viscoelastic material (e.g., Jaeger, 1969) and both displacement and excess fluid-pressure in a poroelastic material (e.g., Wang, 2000). The three-dimensional finite-element model (FEM) consists of two 15-km-thick layers in which a fully coupled poroelastic upper crust overlies a viscoelastic lower crust layer. The upper mantle is implicitly modeled via the boundary conditions as decoupled from the lower crust. The transient response of the model is controlled by two adjustable parameters, (hydraulic) diffusivity in the upper crust and viscosity of the lower crust. A self-consistent set of poroelastic and drained elastic parameters (Wang, 2000) are used in the upper crust and lower crust layers, respectively (Table 1). Our choice of poroelastic parameters is based on the sensitivity analysis performed by Masterlark (2000). The model configuration, shown in Figure 2 and summarized in Table 2, is designed to allow for modifications to test sensitivities to relative fault-zone permeability, fluid-flow boundary con-
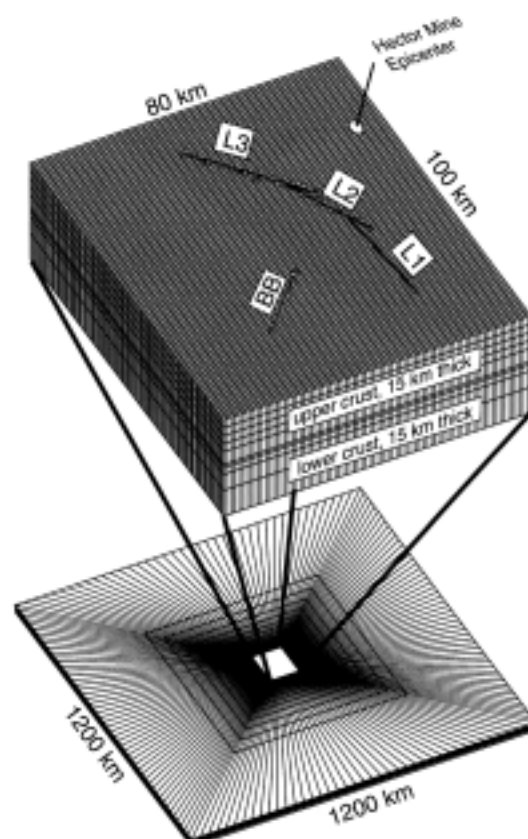

Figure 2.   Finite-element model configuration.

Table 1
Poroelastic Parameters

G	shear modulus (Pa)	1.5×10^{10}
E	Young's modulus (Pa)	3.8×10^{10}
ν	drained Poisson's ratio (dimensionless)	0.25
ν_u	undrained Poisson's ratio (dimensionless)	0.34
K	drained bulk modulus (Pa)	2.5×10^{10}
K_u	undrained bulk modulus (Pa)	4.2×10^{10}
K_s	solid grain modulus (Pa)	4.5×10^{10}
K_f	pore fluid bulk modulus (Pa)	2.3×10^{9}
α	Biot-Willis parameter (dimensionless)	0.47
B	Skempton's coefficient (dimensionless)	0.85
ϕ	porosity (dimensionless)	0.01
S_s	specific storage (m^{-1})	1.8×10^{-7}
E_s	volumetric strain sensitivity coefficient (m)	3.6×10^{6}
μ_f	pore fluid viscosity (Pa-sec)	1.0×10^{-3}
ρ_f	pore fluid density (kg·m^{-3})	10×10^{5}

Table 2
Finite-Element Model Configuration and Specifications, Model A (Preferred Model)

Total Model	
length (explicit)	∞
width (explicit)	∞
thickness (implicit)	∞
number of nodes	124,686
number of elements	109,135
degrees of freedom	453,549
element interpolation	Linear (first order)
solver memory requirement	6.2 Gbytes
initial conditions	$u = 0$ and $\Delta P = 0$
Upper Crust	
thickness	15 km
element layers	6
lateral boundary conditions	$u = 0$ and $\Delta P = 0$
top boundary conditions	$\sigma = 0$ and $\Delta P = 0$
bottom boundary condition	no pore fluid-flow
Lower Crust	
thickness	15 km
element layers	3
lateral boundary conditions	$u = 0$
bottom boundary condition	Foundation, stiffness = 1.5×10^{11} Pa

ditions, elastic parameters, and poroelastic versus elastic upper-crust rheology.

The problem domain in a horizontal plane is separated into three regions centered on the fault trace of the 1992 Landers rupture, which is simplified to consist of three major fault segments: L1, L2, and L3 (Wald and Heaton, 1994) (Fig. 2). The fault trace is bounded for 200 m on either side (Johnson *et al.*, 1997) with elements representing the fault zone. The near-field region, measuring 80 km (east–west) and 100 km (north–south), surrounding the fault zone consists of elements measuring 1 km per side. The far-field region extends the horizontal problem domain to 600 km per side. Elements in this zone gradually increase in size by a factor of 1.2 with distance from the near-field region. A third region bounds the far-field region with infinite elements that simulate exponential decay to zero displacement at infinity.

The fault is a deformable contact surface containing a distribution of 910 contact node pairs. Specified dislocations are applied to contact node pairs along the fault surface (Masterlark *et al.*, 2001) to simulate the 1992 Landers coseismic slip distribution (Wald and Heaton, 1994). The upper surface is an elastic free surface with specified zero excess fluid-pressure, while lateral boundaries are zero displacement and zero excess fluid pressure. The bottom of the poroelastic layer is a no-fluid-flow boundary. The bottom of the lower crust is given a stiffness per unit area, normal to the basal surface, using the material properties of the upper mantle (Turcotte and Schubert, 1982). Due to the relatively short duration (3.5 yr) of postseismic deformation considered in this study, we neglect the viscoelastic flow in the upper mantle based on continental lithosphere strength envelopes (Kohlstedt *et al.*, 1995) and other studies that assume a relatively high upper mantle viscosity (Kaufman and Royden, 1994; Deng *et al.*, 1998; Pollitz *et al.*, 1998) with respect to the viscosity of the lower crust.

The initial stress and fluid-pressure conditions are geostatic. Excess fluid pressure is zero throughout the poroelastic upper crust and there are no deviatoric stresses in the viscoelastic lower crust. These conditions neglect plate-boundary loading (e.g., Deng and Sykes, 1997) and hydraulic stresses due to the hydrologic cycle (e.g., Domenico and Schwartz, 1990). Thermal fluid buoyancy effects are also neglected.

Coseismic Dislocation Load

Undrained conditions exist in the poroelastic upper crust immediately after a sudden dislocation because the coseismic stress is transferred throughout the system much faster than fluids can flow (Wang, 2000). Likewise, the viscoelastic lower crust exhibits a static response to the coseismic load because the time constant for the viscous flow is much larger than the time required for the transfer of coseismic stress. The FEM is constructed to simulate the undrained elastic and elastic (short-time) coseismic response due to a dislocation in the poroelastic and viscoelastic layers, respectively.

Several dislocation-distribution models, restricted to

horizontal slip along vertical fault patches, are available for the Landers rupture (Murray *et al.*, 1993; Freymuller *et al.*, 1994; Hudnut *et al.*, 1994; Johnson *et al.*, 1994; King *et al.*, 1994; Wald and Heaton, 1994). These models vary in complexity from constant slip along a single fault segment (King *et al.*, 1994) to 186 variable dislocation patches distributed over three fault segments (Wald and Heaton, 1994). The dislocation-distribution model selected as the coseismic load for this study, that of Wald and Heaton (1994), is based on geodetic data, strong motion, teleseismic waveforms, and surface-offset measurements. It allows for depth-dependent slip and accounts for the fault step-over geometry of the surface-trace. Because there is evidence for vertical slip components along fault-segment L3 (Arrowsmith and Rhodes, 1994), Deng *et al.*, (1998) suggested a dislocation distribution combining the Wald and Heaton (1994) dislocation distribution with 0.7 m of vertical slip along fault segment L3 to produce postseismic fault-normal surface displacement near the fault zone, which an afterslip model allowing for horizontal slip only could not reproduce (Savage and Svarc, 1997).

Competing Models

Five models are investigated (Table 3). Model A is the preferred model; the other four competing models are constructed to fulfill dual purposes. First of all, the competing models are used for sensitivity analyses. Second, the plausibility of competing model results is used to discriminate

Table 3
Preferred (Model A) and Competing Models (B, C, D, and E)

Model A (preferred model)

upper-crust rheology	poroelastic
slip model	(Wald and Heaton, 1994)
relative fault-zone permeability	1
fluid-flow boundary, top	$\Delta P = 0$

Model B

upper-crust rheology	poroelastic
slip model	(Wald and Heaton, 1994)
relative fault-zone permeability	10^3
fluid-flow boundary, top	$\Delta P = 0$

Model C

upper-crust rheology	poroelastic
slip model	(Wald and Heaton, 1994)
relative fault-zone permeability	0
fluid-flow boundary, top	$\Delta P = 0$

Model D

upper-crust rheology	poroelastic
slip model	(Wald and Heaton, 1994)
relative fault-zone permeability	0
fluid-flow boundary, top	no flow

Model E

upper-crust rheology	elastic
slip model	(Deng *et al.*, 1998)
relative fault-zone permeability	NA
fluid-flow boundary, top	NA

among a variety of conceptual models. Models B and C test the significance of relative fault zone permeability. These models include relatively high and low fault-zone permeabilities, respectively. Model D tests the significance of the fluid-flow boundary condition along the elastic free-surface (Masterlark, 2000). Calibration of model B, with zero excess fluid-pressure specified along the elastic free-surface combined with a relatively permeable fault zone, produces the lower limit for diffusivity. Model D, with no fluid flow specified along the elastic free surface combined with an impermeable fault zone, produces the upper limit for diffusivity. Model E tests sensitivity to upper-crust rheology and is designed to simulate the mechanics and loading described by Deng *et al.* (1998), in which a drained elastic upper crust overlies a viscoelastic lower crust. For model E, the Wald and Heaton (1994) dislocation-distribution used in models A, B, C, and D is combined with an additional 0.7 m vertical dislocation along segment L3.

Predictions from all models are not expected to be precisely comparable to the observed data. First of all, a dislocation distribution for the 1992 Landers rupture does not exist for the boundary conditions and material property specifications of the FEMs considered, although we include the fault-segment geometry of the Wald and Heaton (1994) dislocation distribution. Other studies, using FEMs to predict postseismic deformation also include the Wald and Heaton (1994) dislocation source that is not consistent with the FEM configuration (e.g., Deng *et al.*, 1998; Freed and Lin, 2001). This mismatch between the assumptions of the dislocation distribution and the FEM configuration can introduce significant coseismic and postseismic prediction errors (Masterlark *et al.*, 2001). Second, we consider only two postseismic deformation mechanisms: (1) poroelastic relaxation in the upper crust and (2) viscoelastic relaxation in the lower crust. Postseismic deformation is most likely caused by some combination of these two mechanisms, along with viscoelastic relaxation in the mantle (Pollitz *et al.*, 2000), afterslip (Savage and Svarc, 1997), local heterogeneous effects such as fault zone collapse (Massonnet *et al.*, 1996), and other unknown mechanisms.

Observational Data

Finite-element model predictions are constrained by displacements derived from GPS data and InSAR images. Predicted shallow excess fluid-pressure distributions are compared to borehole strain meter and water-level data. Because coupling between the 1992 Landers and 1999 Hector Mine earthquakes includes transient poroelastic and viscoelastic loading effects, the spatial evolution of Coulomb stress changes along the Hector Mine rupture plane are compared to the hypocenter location.

The allure of InSAR lies in its ability to detect surface deformation on the centimeter scale with high spatial reso-

lution over a large region (Madsen and Zebker, 1998). InSAR images measure deformation as a change in range along the satellite line-of-sight (LOS) direction. The LOS direction for the InSAR images associated with the Landers event is given by the basis vector $\mathbf{n} = [0.33, -0.07, 0.94]$ (Massonnet *et al.*, 1996). We construct synthetic InSAR images by projecting displacement predictions onto the LOS-basis vector.

Although a large pool of relevant GPS data is available for both coseismic and postseismic deformation, two subsets are selected to ensure self-consistency in terms of data processing methods. A subset of coseismic displacement data reported for 92 stations in southern California (Hudnut *et al.*, 1994) constrains the coseismic FEM predictions. The 19 stations given in Table 4 are sufficient to characterize horizontal coseismic deformation in the near-field region of the model. These stations are located in a square region with sides measuring roughly 100 km centered on the Landers rupture trace. Outside of this region, coseismic displacement magnitudes decrease dramatically and do not usefully constrain the model.

Data from the 11 GPS stations shown in Figure 1b are selected for the transient calibration and are also used for other postseismic deformation studies of incremental displacements following a time-step of 3.4 years (Savage and Svarc, 1997; Deng *et al.*, 1998; Peltzer *et al.*, 1998; Pollitz *et al.*, 2000). The stations transect fault segment L3 and are located in a region with the largest expected magnitudes of poroelastic deformation (Peltzer *et al.*, 1998; Masterlark, 2000). The time-series deformation data from these stations are shown in Figure 3. Although these 11 stations represent a relatively sparse array of spatial observational data, they are sufficient to constrain the transient behavior of the model due to their locations.

Both water level and borehole strain data can be used to constrain dilatation predictions. For undrained conditions, the change in water level (hydraulic head) is equal to the dilatation scaled by a volumetric strain sensitivity coefficient (Wang, 2000). Water level and borehole strain data must be used with care for a variety of reasons. First, the data are collected from wells and boreholes with depths limited to a maximum of a few hundred meters. Hence, the data sample only a veneer of the 15-km-thick poroelastic upper crust. Because we assume a bulk poroelastic upper crust, water level and borehole strain data sample a different spatial scale and may reflect properties unique to the near-surface. Furthermore, many of the wells and boreholes are located near the nodal planes of the 1992 Landers strain field. Because volumetric strain gradients are greatest near these planes, small errors in predictions result in large differences with respect to observed data. Significant differences in observed coseismic water-level changes and water-level changes predicted from elastic dislocation models have been reported in other studies (e.g., Roeloffs, 1995; Masterlark *et al.*, 1999). Relevant water-level and borehole strain-meter data are summarized in Table 5.

Table 4
Coseismic Horizontal GPS Displacement

Station	Coordinates		Model Location* (m)		Displacement† (m)	
	lat, °N	lon, °W	east (x)	north (y)	u_x	u_y
6050	34.266	116.334	7812	20,666	0.495 ± 0.095	-0.480 ± 0.037
6052	34.516	116.840	$-39,196$	48,368	-0.374 ± 0.074	0.029 ± 0.052
6054	34.204	116.442	-1853	13,779	0.101 ± 0.080	1.293 ± 0.035
6056	34.370	116.647	$-21,361$	32,202	-0.097 ± 0.070	0.663 ± 0.036
6058	34.040	116.585	$-15,835$	-4458	0.136 ± 0.090	0.333 ± 0.053
6060	34.136	116.329	7959	6175	0.429 ± 0.099	-0.284 ± 0.074
7000	34.676	116.716	$-27,584$	66,190	-0.955 ± 0.177	0.154 ± 0.057
7001	34.560	116.469	-5057	53,339	0.383 ± 0.053	-1.202 ± 0.030
7007	34.705	116.225	17,631	69,437	0.0170 ± 0.062	-0.227 ± 0.035
BEAR	34.264	116.884	$-43,209$	20,347	-0.042 ± 0.003	0.099 ± 0.003
CHER	34.003	116.952	$-49,367$	-8708	0.041 ± 0.015	0.154 ± 0.021
DUMP	34.793	116.663	$-22,834$	79,204	-0.284 ± 0.168	-0.100 ± 0.058
HECT	34.785	116.421	-2165	78,343	-0.068 ± 0.005	-0.324 ± 0.005
INA5	34.004	116.515	-9648	-8440	0.101 ± 0.008	0.267 ± 0.008
LAZY	34.344	116.514	-9353	29,321	-0.103 ± 0.003	1.697 ± 0.003
MAUM	34.419	116.458	-4031	37,670	0.576 ± 0.005	-1.667 ± 0.005
MEEK	34.258	116.617	$-18,548$	19,762	0.239 ± 0.007	0.656 ± 0.006
ONYX	34.193	116.710	$-27,064$	12,519	0.235 ± 0.052	0.339 ± 0.023
SANH	34.255	116.279	12,592	19,439	0.411 ± 0.005	-0.309 ± 0.004

From Hudnut *et al.*, 1994.
*Southern tip of fault-segment L1 is the origin.
†± 1 standard deviation.

Postseismic Deformation of the 1992 Landers Earthquake

Two types of physical models explaining postseismic surface deformation due to accumulated shear stress beneath the coseismic rupture are (1) aseismic afterslip and (2) viscoelastic relaxation (Shen *et al.*, 1994). Aseismic afterslip models have time-dependent slip along a plane downdip from the coseismic rupture and often include HEHS assumptions (Savage, 1990). The simplest postseismic viscoelastic relaxation models include an elastic layer over a viscoelastic layer, although multilayer systems are available (Deng *et al.*, 1998; Pollitz *et al.*, 2000). For the simple two-layer case, shear stress relaxes through broad deformation of the viscoelastic layer, which causes deformation in the overlying elastic layer. The fundamental difference between afterslip and viscoelastic relaxation models is whether or not relaxation of the coseismic shear stress is confined to a plane beneath the coseismic rupture. The resulting surface deformations from the two models are generally indistinguishable from one another, and afterslip models are often chosen for computational simplicity and amenability to formal inversion schemes (Savage, 1990; Savage and Svarc, 1997).

From a modeling perspective, viscoelastic relaxation is a more natural approach to addressing the relaxation of coseismic shear stress, because the driving mechanism is explicitly derived from the coseismic dislocation load. For the case of the 1992 Landers earthquake, Deng *et al.* (1998) constructed a viscoelastic relaxation model constrained by both GPS data and an InSAR image. To produce the observed fault-normal postseismic displacements, a vertical component of coseismic slip is included. Although the model successfully predicts observed fault-normal displacements at a time-step of 3.4 yr, we will show that their model (our model E) is unable to account for transient displacements. An alternative model using viscoelastic relaxation of the upper mantle (Pollitz *et al.*, 2000) successfully predicts the postseismic InSAR image and far-field GPS displacements; however, that model does not predict horizontal GPS displacements very well for locations near the Landers rupture. We did not test the transient response of the model proposed by Pollitz *et al.* (2000) because the configuration is significantly different from our FEM.

For the Landers earthquake, displacements predicted by afterslip models are relatively consistent with observed deformation (Shen *et al.*, 1994; Savage and Svarc, 1997). Generally, the spatial distributions of surface deformation predicted by the afterslip models are similar to those for the coseismic phase, although the postseismic deformation is of a lesser magnitude and occurs over a broader area. Predicted postseismic horizontal-surface displacements (a few tens of centimeters) for the 3.4-yr period following the coseismic rupture are subparallel to the fault-slip plane. However, an afterslip model does not reproduce the fault-normal displacements observed within a few kilometers of the fault zone (Savage and Svarc, 1997).

Horizontal deformation normal to the fault and nodal planes is a characteristic regional scale poroelastic relaxation response following strike-slip rupture (Peltzer *et al.*, 1998).
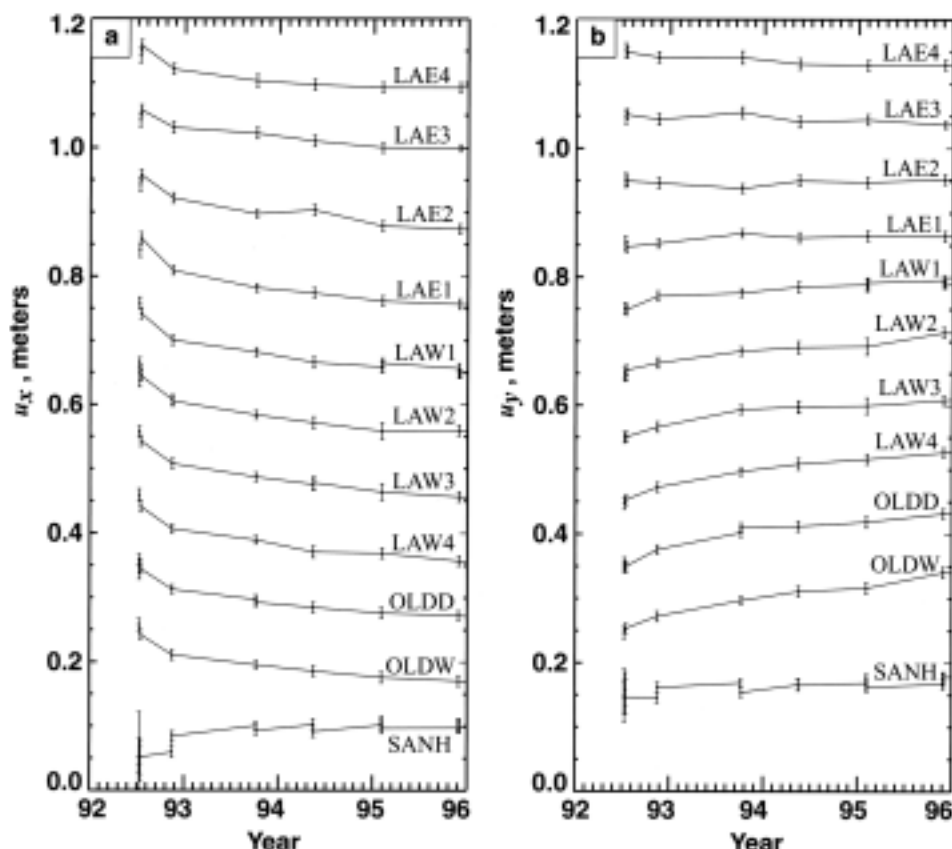
Figure 3.   Postseismic horizontal GPS displacement time-series data. These data are from USGS website: *http://quake.wr.usgs.gov:80/QUAKES/geodetic/gps/LandersPro* (2000). The data are corrected for secular strain (discussed in the text) and shown with respect to a fixed North American plate plus an arbitrary constant value. Error bars are ± 1 standard deviation. (a) u_x. (b) u_y.

The occurrence of this fault-normal deformation suggests poroelastic effects are not limited to the fault zone region (Massonnet *et al.*, 1996; Peltzer *et al.*, 1996; Bosl and Nur, 1998) and must be included as a regional-scale, postseismic deformational mechanism. Peltzer *et al.* (1998) pointed out that a synthetic InSAR image from either the afterslip solution or poroelastic effects is inconsistent with the actual InSAR image for the ~3-yr period following the Landers rupture and combined both poroelastic and afterslip deformation with superposition. The superposition is not self-consistent, however, because the afterslip distribution (Savage and Svarc, 1997) is derived from GPS displacements that contain significant poroelastic deformation components. In this study, we assume regional deformation following the 1992 Landers earthquake is caused by poroelastic and viscoelastic relaxation in the upper and lower crust layers, respectively.

Half-Space Approximation for Poroelastic Relaxation

An analytical solution is available for displacement and its spatial derivatives due to specified displacement along a rectangular fault in an HEHS (Okada, 1992). A complete quasistatic deformation solution for the 1992 Landers rupture is the superposition of solutions for dislocation along each of the 186 fault patches from the Wald and Heaton (1994) dislocation distribution. The undrained Poisson's ratio ($\nu_u = 0.34$) is used to simulate the quasistatic coseismic response. For the drained (steady-state postseismic) condition, coseismic excess fluid pressures have dissipated completely and the drained Poisson's ratio ($\nu = 0.25$) is used in the calculations. Steady-state conditions represent the equilibrium response of the system to slip along the fault. Total postseismic poroelastic deformation is estimated by taking the difference between the solutions determined for drained and undrained conditions (Fig. 4).

The HEHS model of strike-slip dislocation of the 1992 Landers earthquake predicts a quadrantal pattern of compression and dilatational regions. This juxtaposition of compression and dilatation across the nodal and fault planes enhances horizontal postseismic poroelastic displacement normal to these planes. In the quadrants of coseismic compression, positive excess fluid pressure decays to equilibrium, inducing a regional contraction. The opposite effect occurs in the coseismic dilatational regions. A maximum

Table 5
Coseismic Water-Level Changes and Borehole Strain

Station	Coordinates		Model Location* (m)		Change in water level, Δh (m)
	lat, °N	lon, °W	east	north	
from near-field region (Roeloffs *et al.*, 1995)					
GR	34.870	117.938	−140,190	86,730	0.42
FS5	34.849	117.837	−130,880	84,533	0.11
HO1	34.810	117.887	−135,504	80,133	0.16
HO2	34.810	117.887	−135,504	80,133	0.16
LCV	34.531	116.906	−45,188	50,008	3.00
SBV	34.078	117.294	−80,889	−570	0.003
MBP	34.104	117.286	−80,138	2326	0.33
GP	34.115	117.311	−82,443	3528	0.42
JWR	33.592	116.458	−4076	−54231	0.09
from Pinon Flat Observatory (PFO) (Wyatt *et al.*, 1994)†					
CIA	33.612	116.458	−3342	−52,007	−0.15
CIB	33.612	116.458	−3342	−52,007	−0.20
CIC	33.612	116.458	−3342	−52,007	−0.60
UQA	33.612	116.458	−3342	−52,007	−5.0
from SAF zone borehole strain (Johnston *et al.*, 1994)					
PUB	34.433	117.883	−135,092	38,252	1.8‡

*Southern tip of fault-segment L1 is the origin
†Locations given are for GPS station PIN1.
‡Measured ε_{kk} is 4.9×10^{-7} and $\Delta h = E_s \varepsilon_{kk}$.

horizontal displacement of 0.18 m is predicted normal to fault segment L3, which illustrates that the GPS stations used for postseismic deformation constraints (Fig. 1b) are ideally located. Similar fault-normal displacement (about 0.1 m) is predicted for locations near fault segment L1. Calculated horizontal displacements are minimal near the regions of high coseismic excess fluid pressure. Conversely, the greatest vertical poroelastic displacement (a few centimeters) is predicted for regions near the greatest coseismic excess fluid pressure. Predicted vertical deformation is suppressed near the nodal and fault planes.

FEM Method

The coseismic distributions of poroelastic and elastic state variables predicted for the upper and lower crust, respectively, serve as the initial conditions for the transient simulation. The general characteristics of the predicted coseismic surface deformation are shown in Figure 5. Horizontal deformation is characterized by increasing displacement tangential to the coseismic dislocation with proximity to the fault zone. The horizontal displacement is generally convergent in the dilatational quadrants and divergent in the compressive quadrants with respect to the fault zone. The vertical displacement forms a quadrantal pattern of uplift and subsidence regions bounded by the fault and nodal planes. More complex displacement patterns occur near the fault zone due to the nonuniform dislocation distribution and fault step-over geometry.

Deviatoric stress from the coseismic dislocation load transferred throughout the lower crust drives subsequent viscoelastic relaxation. Viscoelastic relaxation occurs if the deviatoric stress is nonzero anywhere within the viscoelastic material. Von Mises stresses with magnitudes in excess of 20 MPa exist in the lower crust beneath the fault zone region and are not confined to a plane downdip from the rupture surface (Fig. 6). These stresses decay rapidly with distance from the fault zone in both horizontal and vertical directions.

The predicted coseismic displacements from model A are in good agreement with observed GPS data (Fig. 7). Pre-
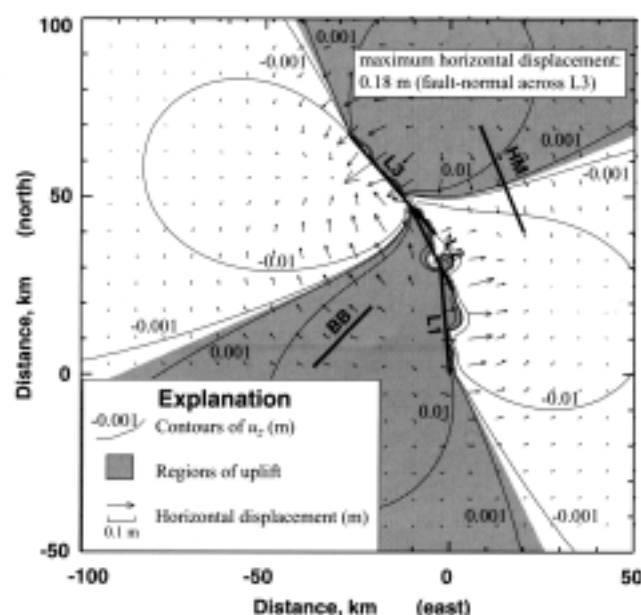

Figure 4.   Poroelastic relaxation, analytical solution.
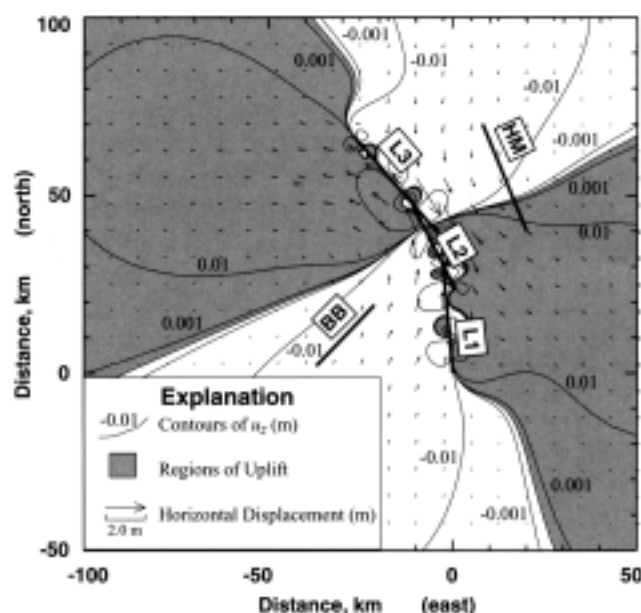
Figure 5.   FEM-predicted coseismic surface displacement.
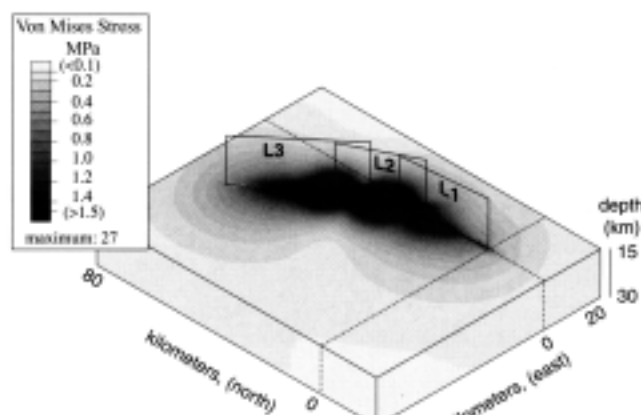

Figure 6.   Predicted von Mises stress, lower crust. The fault planes in the overlying upper crust are shown for spatial reference.

dictions from models B, C, and D are identical to the preferred model, because fault-zone permeability and fluid-flow boundary condition specifications are irrelevant during the undrained response. Model E predictions are also very similar to the preferred model, although careful examination reveals small differences, particularly in predictions near the Landers rupture trace.

The coseismic InSAR image is dominated by a large displacement lobe in the northwest quadrant of the near-field region (Fig. 8), where about 20 fringes can be identified in both actual and synthetic InSAR images. Each fringe corresponds to 0.028 m of displacement in the LOS direction, for a total LOS displacement of 0.56 m near the fault trace (Mas-

sonnet *et al.*, 1993). A smaller displacement lobe occurs in the near-field east of fault segment L2. Line-of-Sight displacements are suppressed in the southwest and northeast quadrants, since the general sense of displacement is orthogonal to the basis vector in these quadrants. This does not suggest that less displacement occurred, but that InSAR images are most sensitive to displacement subparallel to the LOS direction. Predictions from models A, B, C, and D are in good agreement with the InSAR image. Model E contains a feature with concentric fringes, which is inconsistent with the actual image, southwest of the fault segment L1.

Excess fluid-pressure calculated for a depth of 2.5 km and observed water-level changes are shown in Figure 9. The distribution of excess fluid pressure is dominated by the expected quadrantal pattern of contraction and dilatation zones bounded by the fault and nodal planes. Zones of significant excess pressure, greater than 10 m of head, exist in the near-field region and are not confined discontinuities in the fault trace. We shall show that the extensive distribution of the coseismic excess fluid pressure combined with the juxtaposition of positive and negative excess-fluid-pressure regions separated by relatively sharp gradients have a significant impact on postseismic displacement and Coulomb stress as the excess fluid pressure decays. Predicted results are consistent with observed coseismic water-level changes in terms of both magnitude and phase, with the exception of well JWR.

For the postseismic simulation, the model is calibrated in terms of transient displacement with respect to GPS time-series data over a period of 3.4 yr following the 1992 Landers earthquake. Because secular loading is not included in the FEM boundary conditions, observed GPS displacements are corrected for reported secular displacement velocities prior to the 1992 Landers event (Feigl *et al.*, 1993; Gordon *et al.*, 1993) using linear interpolations (Masterlark, 2000). The GPS stations are several tens of kilometers from the plate-boundary faults and cumulative corrections are relatively small for a period of a few years.

Calibration parameters are viscosity of the lower crust and diffusivity of the poroelastic upper crust. Time-dependent solutions are determined for 1.0 months, 2.0 months, 6.0 months, 1.0 yr, 2.8 yr, and 3.4 yr following the coseismic response. This time sequence corresponds to the temporal GPS data (Fig. 3). A two-step calibration approach is used. First, the lower-crust viscosity is calibrated to the long-term (a few years) displacement, assuming most of the excess fluid pressure decays over a relatively shorter time period. The diffusivity is then calibrated to the short-term (a few months) transient displacement using the calibrated viscosity.

The predicted postseismic horizontal displacements are also compared to observed GPS data for a time-step of 3.4 yr, neglecting intermediate time-series data, to allow for direct comparison with the postseismic deformation study by Deng *et al.* (1998) (Fig. 10). The FEM predictions for all 10 GPS displacements indicate a displacement magnitude on the order of 10 cm over the 3.4-yr time period. The magnitudes
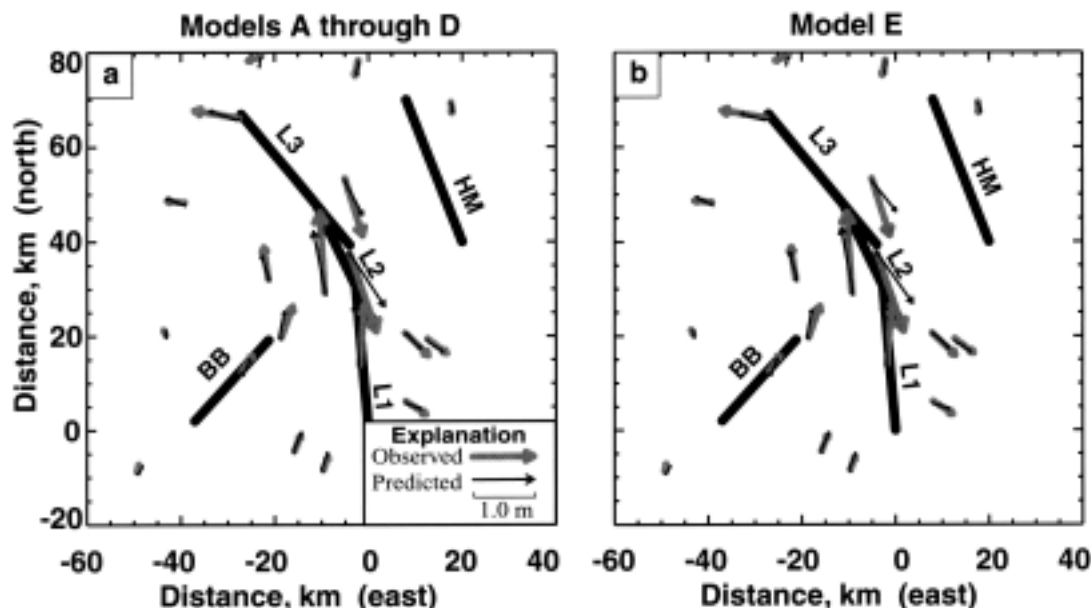
Models A through D **Model E**

Figure 7.   Observed and predicted coseismic surface displacement. The explanation applies to both figures in this composite. (a) Models A, B, C, and D. Predictions for these models are identical because specifications of fault-zone permeability and fluid-flow boundary conditions do not affect the coseismic (undrained) response. (b) Model E. The predictions are similar to those from models A, B, C, and D; however, subtle differences are visible.
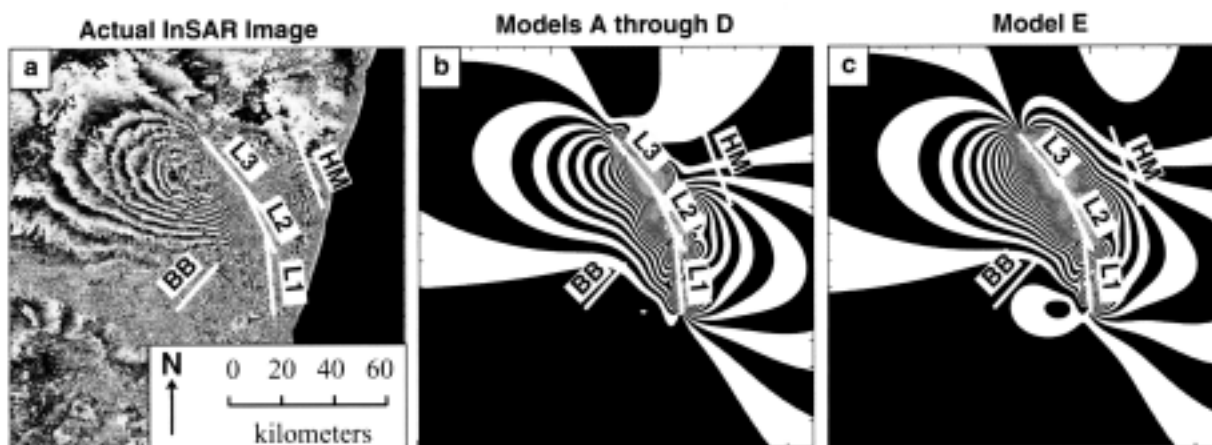
Actual InSAR Image **Models A through D** **Model E**

Figure 8.   Actual and synthetic coseismic InSAR images. Each fringe, black–white–black, represents 2.8 cm of displacement in the LOS direction. (a) The actual InSAR image is generated between April and July of 1992 (Massonnet *et al.*, 1993). (b) A synthetic image is developed from FEM predictions from models A, B, C, and D. (c) Model E. The feature southwest of fault segment L1 is distinctly different from the actual image and the preferred model synthetic image.

of the predictions are in better agreement than the directional components, particularly near fault segment L3. The model proposed by Deng *et al.* (1998) (our model E) agrees slightly better, compared to predictions from the other competing models, with observed displacements for this time-step. Overall, each competing FEM predicts the pattern of observed horizontal deformation and the fault-normal displacement observed close to fault segment L3. This is an improvement over the afterslip model proposed by Savage and Svarc (1997), which predicts minimal fault-normal deformation for the corresponding time-step. Comparison among synthetic InSAR images generated by the competing models is relatively inconclusive.

Transient displacement is calibrated with respect to the magnitude of horizontal displacement (u_e), because comparison to the individual displacement components (u_x and u_y)
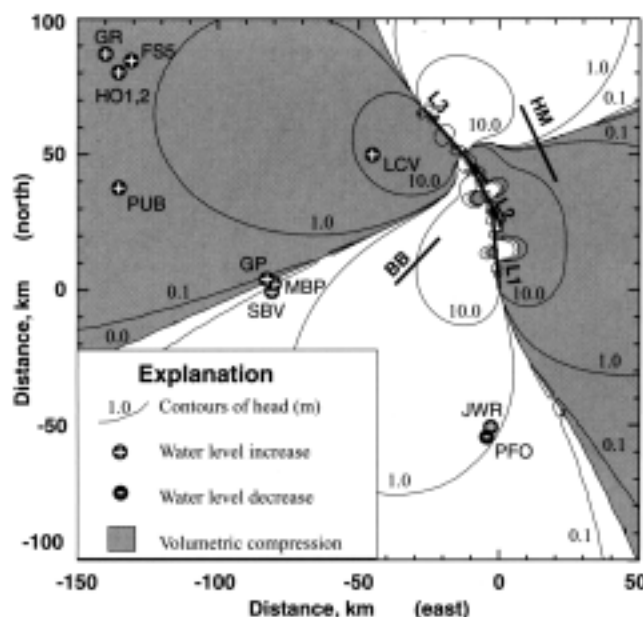
Figure 9.   Predicted coseismic excess fluid-pressure distribution. The excess fluid-pressure response is calculated for a depth of 2.5 km. The model response to the strike-slip dislocation has a quadrantal pattern of compressional (shaded regions) and dilatational zones. Observed water-level changes are summarized in Table 5.

is unsatisfactory due to the directional mismatch shown in Figure 10. GPS station SANH contains the most comprehensive data set for the time-period, and is the only time-series with temporal measurements common to all of the other stations. The time-series from the 10 GPS stations transecting fault segment L3 are differenced with respect to GPS station SANH, to remove spatially correlated noise (Fig. 3). The calibration was performed visually, because a more rigorous statistical analysis (e.g., weighted mean square error) would not be appropriate due to the bias in model predictions discussed in the Competing Models section.

The long-time response occurs during the later portion of the 3.4-yr interval following the Landers rupture. Diffusivity is specified to be sufficiently high (10^5 m^2·sec^{-1}) to force a relatively instantaneous poroelastic response during the first time-step (a period of 1.0 month). The predicted long-time (~2.8–3.4 yr) displacement behavior is then calibrated by varying the lower crust viscosity parameter. Predictions from model A with specified viscosities of 4×10^{18} and 6×10^{18} Pa·sec provide limits for the calibrated viscosity of 5×10^{18} Pa·sec. Because the poroelastic response occurs during relatively short time periods, the long-time calibration of viscosity is insensitive to variations in fault-zone permeability and fluid-flow specifications given in competing models B, C, and D (Fig. 11). Theoretically, the poroelastic response from model C should be slightly lower, because the impermeable fault-zone elements will not contribute to poroelastic relaxation; however, the relative vol-

ume of the fault-zone elements is small compared to the problem domain. For model E, the calibrated lower-crust viscosity is 3×10^{18} Pa·sec (Fig. 12).

The diffusivity is calibrated to the short-time observed deformation, using the lower-crust viscosity from the long-time calibration (5×10^{18} Pa·sec) determined above. Model A displacement predictions, using diffusivities of 10^{-1} m^2·sec^{-1} and 10^{-3} m^2·sec^{-1}, provide the upper and lower bounds for the calibrated diffusivity. Although a variety of diffusivities within this range can characterize an individual station, a diffusivity of 10^2 m^2·sec^{-1} fit all of the stations reasonably well (Fig. 13). This diffusivity also fits best for competing models B (lower-limit configuration), C, and D (upper-limit configuration). The data from the stations nearest the fault zone (LAW1 and LAE1) show the largest displacements within the first few months following the coseismic event. If the short-time response is calibrated only to displacements observed at these two GPS stations, which are most sensitive to poroelastic deformation (Fig. 4), then the calibrated diffusivity is closer to 10^{-3} m^2·sec^{-1} for models A, B, C, and D. Model E, proposed by Deng *et al.* (1998), cannot simulate the transient behavior of the system.

The poroelastic and viscoelastic contributions to surface deformation, predicted with model A, are shown in Figure 14. The FEM poroelastic prediction is similar to the analytical solution (Fig. 4). The primary difference between the two is the general reduction in magnitude for FEM predictions due to the differences in boundary conditions. The analytical solution assumes an infinitely thick poroelastic layer, whereas the FEM has a finite poroelastic layer thickness (15 km). Furthermore, the base of the FEM is decoupled from the upper mantle.

The viscoelastic contribution is dominated by horizontal deformation similar to the coseismic response, but distributed over a broader region because viscoelastic relaxation occurs deeper than the coseismic dislocation load. The greatest displacements are subparallel to the fault planes near the rupture segments. The magnitude of vertical deformation is minimal. Neither the poroelastic nor viscoelastic components that we tried, taken individually, can characterize postseismic deformation.

Evolution of Coulomb Stress near the 1999 Hector Mine Earthquake Hypocenter

A change in Coulomb stress is a quantitative estimation of the change in the tendency for frictional slip to occur along a locked, pre-existing fault:

$$\Delta\sigma_C = \Delta\sigma_S + f(\Delta\sigma_n + \Delta P), \qquad (1)$$

where $\Delta\sigma_C$ is the change in Coulomb stress, f is a coefficient of friction, $\Delta\sigma_S$ and $\Delta\sigma_n$ are incremental changes in shear stress aligned with the dislocation vector along a fault and fault-normal stress (tension positive), respectively, and ΔP
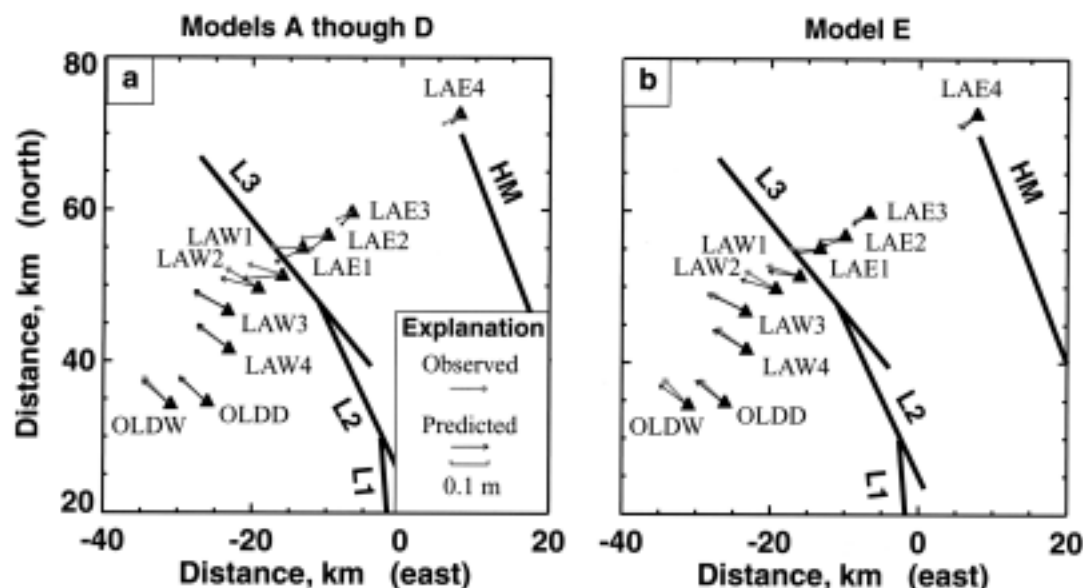
Models A though D

Model E

Figure 10. Postseismic horizontal displacement. Observed and predicted displacements are similar for a time-step of 3.4 yr. (a) Models A, B, C, and D. (b) Model E.
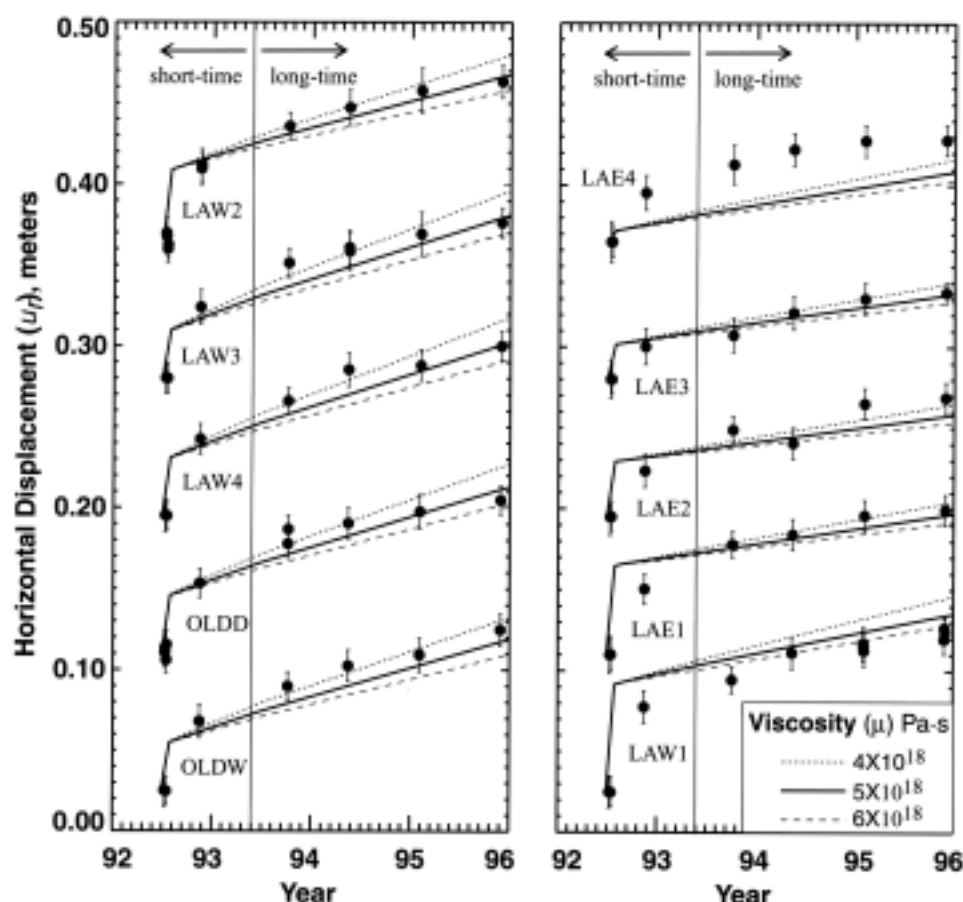
Figure 11. Long-time FEM transient calibration, models A, B, C, and D. Because the poroelastic response is assumed to be a short-term occurrence, the long-term predictions from models A, B, C, and D are the same. The models are calibrated to GPS horizontal displacement magnitude data from Fig. 3, differenced from GPS station SAHN. An instantaneous poroelastic response is forced during the initial time-step.
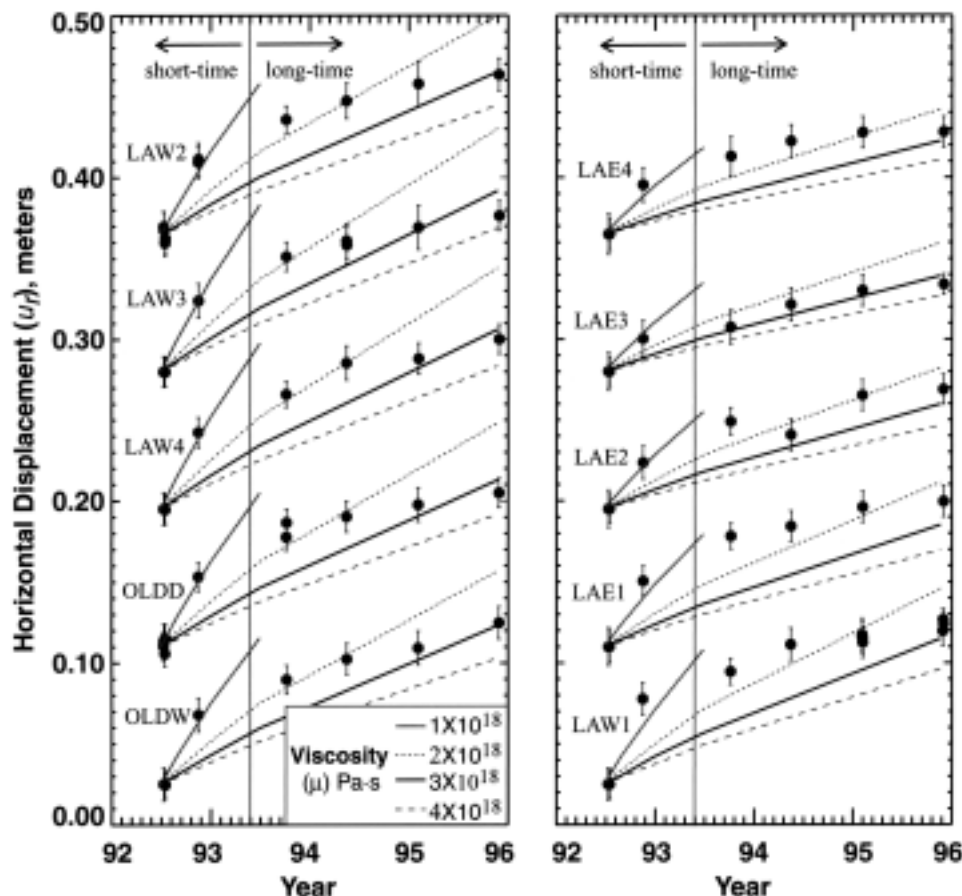
Figure 12.   Long-time FEM transient calibration, model E. Data are taken from Fig. 3 as described in Fig. 11. A viscosity of 3×10^{18} Pa·sec fits the long-time (1996) data best, however the viscosity chosen for this model is dependent upon the time-step.

is the excess fluid pressure (e.g., Roeloffs, 1995). Static-stress-coupling analyses of the causal relationship between earthquakes are applicable either for short time periods (undrained conditions) or long time period (drained conditions) following a dislocation (Wang, 2000). We allow for time dependence in state variables because of transient poroelastic and viscoelastic relaxation.

The spatial and temporal characteristics of hypocenters are the observational data most directly predicted by Coulomb stress. The calibrated FEM is used to quantify the evolution of Coulomb stress changes, initiated by the 1992 Landers rupture, near the 1999 Hector Mine hypocenter and to estimate the coupling between the two events (Fig. 15). Significant coupling is expected, because the epicenter of the Hector Mine earthquake is located within a distance of a few fault-widths from the Landers rupture. For the case of the Hector Mine earthquake, a simple north-northwest-trending fault plane is assumed (Hurst et al., 2000). The epicenter is located along the northern end of the fault plane (Parsons and Dreger, 2000). The predicted change in Coulomb stress along the rupture plane of the Hector Mine earthquake is estimated for fault planes dipping 90° (Hurst et al.,

2000) and 77° (Parsons and Dreger, 2000) east. The reported hypocentral depth is about 5 km (Dreger and Kaverina, 2000; Parsons and Dreger, 2000; Scientists of the USGS et al., 2000) and calculations are performed for depths of 3.75 and 6.25 km because of the FEM configuration. Solutions are insensitive to variations in both dip and hypocentral depth that we tested.

Predicted Coulomb stress changes near the Hector Mine earthquake hypocenter increase from 0.02 MPa (1992 Landers coseismic response) to 0.05 MPa (immediately preceding the 1999 Hector Mine earthquake). This increase in Coulomb stress is primarily due to the recovery of decreased excess fluid pressure from the 1992 Landers coseismic strain field (Fig. 9). The magnitude of the transient change in Coulomb stress is significant (Masterlark and Wang, 2000) and is consistent with earthquake probabilities based on seismicity data (Wyss and Wiemer, 2000). Studies indicating that the 1999 Hector Mine earthquake occurred in the stress shadow of the 1992 Landers earthquake (e.g., Hauksson et al., 1999; Wyss et al., 1999) neglect significant transient effects, including poroelastic effects, during the 7-year period separating the two events.
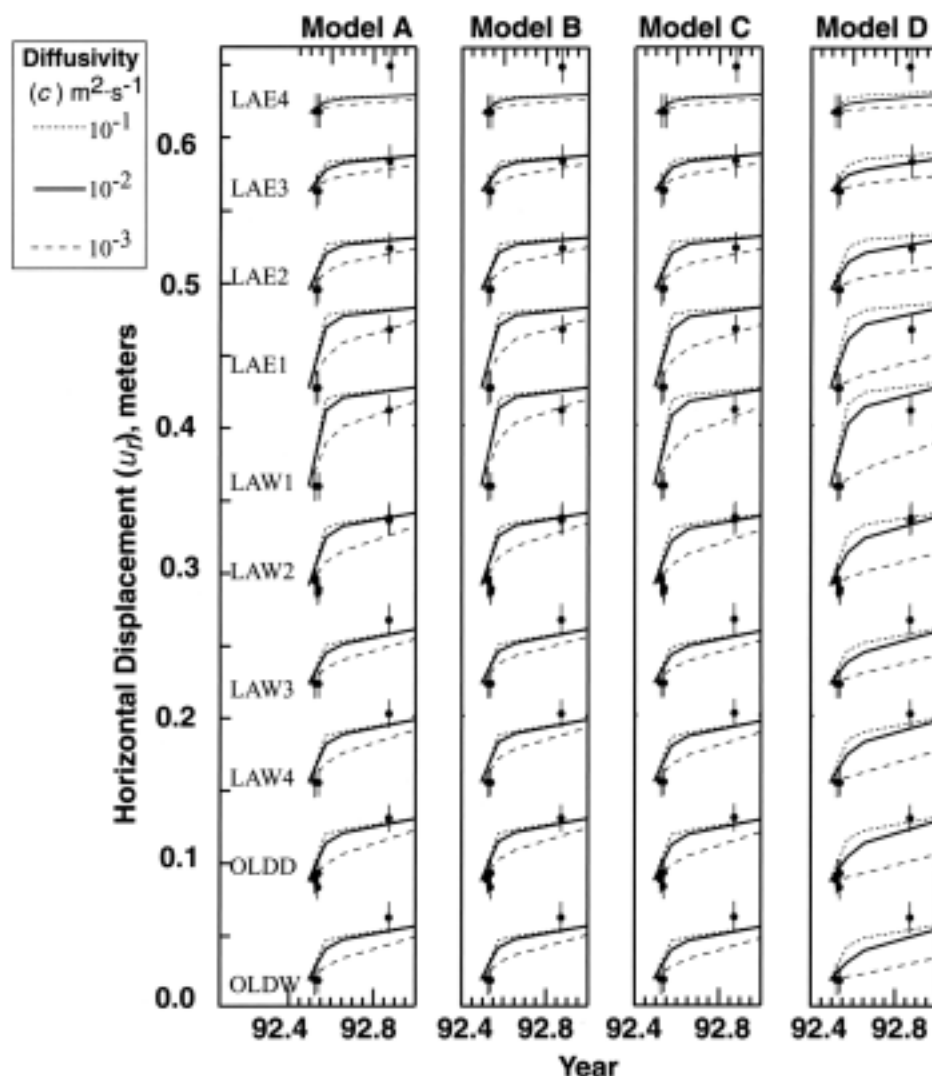
Figure 13.   Short-time FEM transient calibration. Data are taken from Fig. 3 as described in Fig. 11. The diffusivities for models A, B, C, and D are calibrated to short-time deformation data.

Conclusions

Our preferred model (model A) explicitly treats the crust as a system of homogeneous isotropic poroelastic and viscoelastic layers. The relatively simple conceptual model is capable of simulating transient deformation on a regional scale, with only two adjustable parameters (viscosity of the lower crust and diffusivity in the upper crust). This represents an alternative to complicated half-space afterslip models with numerous adjustable parameters and HEHS assumptions.

Two calibration parameters are constrained to within a high level of precision. Lower-crust viscosity, 5×10^{18} Pa·sec, is determined to within a significant digit; upper-crust diffusivity is calibrated to lie within a surprisingly tight range of 10^{-2} to 10^{-3} m^2·sec^{-1}, depending on fluid-flow specifications and boundary conditions. This suggests that

our model is relatively insensitive to the choice of either no fluid flow or zero excess fluid pressure boundary conditions along the top of the problem domain. Based on near-field poroelastic deformation only, Peltzer *et al.* (1996) reported a diffusivity on the order of 1 m^2·sec^{-1} for the step-overs between the three 1999 Landers rupture segments. This is significantly higher than the values we determined based on GPS near-field stations LAW1 and LAE1. The diffusivity for the rock sample from which the poroelastic parameters are taken (Table 1) is 10^{-1} m^2·sec^{-1} (Wang, 2000). The difference in spatial scales may explain this discrepancy, although the trend is not consistent. Most likely, the higher value reported by Peltzer *et al.* (1996) is due to local heterogeneity.

Predictions from model E, based on Deng *et al.* (1998), are consistent with observed GPS displacements for a single
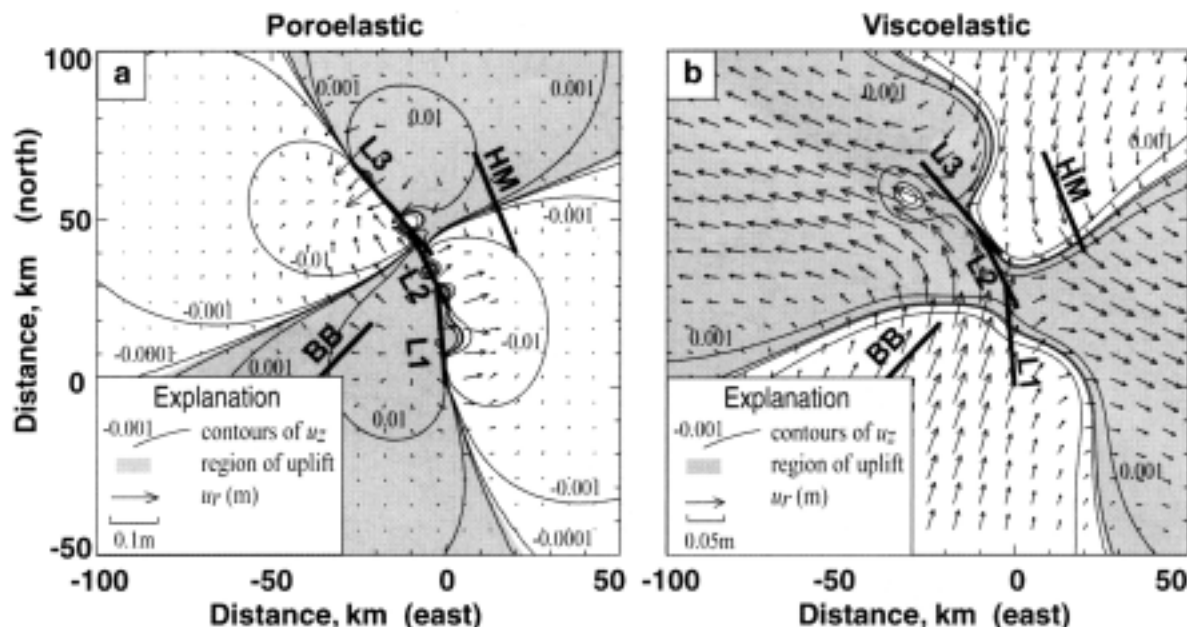
Figure 14. Separate poroelastic and viscoelastic relaxation components, model A. Solutions shown for the elastic free-surface are determined for a time-step of 3.4 yr. (a) Poroelastic deformation. (b) Viscoelastic deformation.
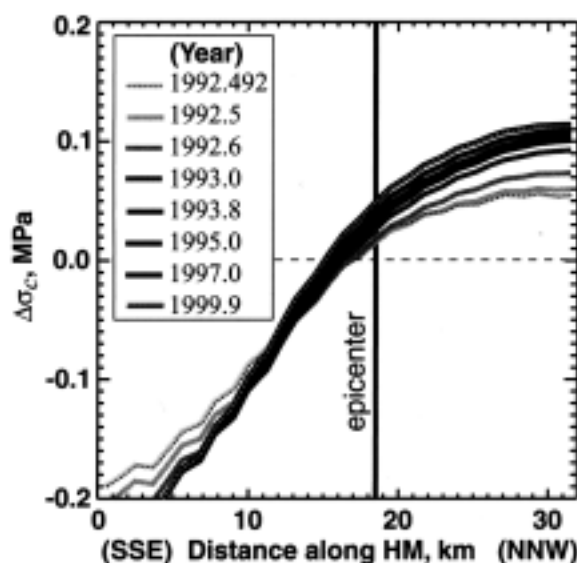

Figure 15. Evolution of Coulomb stress, Hector Mine earthquake. The change in Coulomb stress along the Hector Mine rupture plane (from the SSE end to the NNW end) increased more than 100% near the epicenter during the 7-yr interval following the 1992 Landers earthquake.

time-step of 6 months is chosen instead of 3.4 yr, the apparent viscosity for model E would be 1×10^{18} Pa·sec (Fig. 12).

Deng and Sykes (1997) conducted static coupling analyses for faults in southern California with superposition of HEHS solutions. Their study includes 200 years of secular loading along with dislocations from large earthquakes. A result of the study is a regional seismic hazard forecast that suggests the next $M_w > 7$ earthquake, following the 1992 Landers event, in southern California would occur along the southern portion of the SAF within the next 50 years. The model failed its first post-audit, however, by not predicting the 1999 M_w 7.1 Hector Mine earthquake in the Mojave block.

Masterlark and Wang (2000) point out that changes in Coulomb stress are often calculated using the assumption that fluid pressures are proportional to the fault-normal stress, rather than the mean-normal stress used in standard poroelastic theory. Furthermore, these calculations often include drained material property specifications, an assumption inconsistent with the inclusion of nonzero fluid-pressure effects implied by effective coefficients of friction (e.g., Coulomb 2.0 [Toda *et al.*, 2001]). Coulomb stress calculations require precise determinations of stress and fluid pressure, both of which can evolve significantly over time.

time-step. Although model E simulates observed GPS deformation for the 3.4-yr time-step with a lower-crust viscosity of 3×10^{18}, it cannot match the short-time deformation because the initial transient response is not large enough. The lower-crust viscosity determined for model E is therefore dependent on the chosen time-step. For example, if a

Acknowledgments

References

Arrowsmith, J. R., and D. D. Rhodes (1994). Original forms and initial modifications of the Galway Lake road scarp formed along the Emerson fault during the 28 June 1992 Landers, California earthquake, *Bull. Seism. Soc. Am.* **84,** 511–527.

Bennett, R. A., J. L. Davis, and B. P. Wernicke (1999). Present-day pattern of Cordilleran deformation in the western United States, *Geology* **27,** 371–374.

Bosl, W., and A. Nur (1998). Numerical simulation of postseismic deformation due to pore fluid diffusion, in *Poromechanics,* J.-F. Thimus, Y. Abousleiman, A. H.-D. Cheng, O. Coussy, and E. Detournay (Editors), Balkema, Rotterdam, 23–28.

Deng, J., and L. R. Sykes (1997). Evolution of the stress field in southern California and triggering of moderate-size earthquakes: a 200 year perspective, *J. Geophys. Res.* **102,** 9859–9886.

Deng, J., M. Gurnis, H. Kanamori, and E. Hauksson (1998). Viscoelastic flow in the lower crust after the 1992 Landers, California, earthquake, *Science* **282,** 1601–1772.

Dokka, R. K. (1980). Late Cenozoic tectonics of the central Mojave Desert, California, *Ph.D. Thesis,* University of California, Los Angeles.

Domenico, P. A., and F. W. Schwartz (1990). *Physical and Chemical Hydrogeology,* John Wiley and Sons, New York, 824 pp.

Dreger, D., and A. Kaverina (2000). Seismic remote sensing for the earthquake source process and near-source strong shaking: a case study of the October 16, 1999 Hector Mine earthquake, *Geophys. Res. Lett.* **27,** 1941–1944.

Feigl, K. L., D. C. Agnew, Y. Bock, D. Dong, A. Donnellan, B. H. Hager, T. A. Herring, D. D. Jackson, T. H. Jordan, R. W. King, S. Larsen, K. M. Larsen, M. H. Murray, Z. Shen, and F. H. Webb (1993). Space geodetic measurements of crustal deformation in central and southern California, 1984–1992, *J. Geophys. Res.* **98,** 21,677–21,712.

Freed, A. M., and J. Lin (2001). Delayed triggering of the 1999 Hector Mine earthquake by viscoelastic stress transfer, *Nature* **411,** 180–183.

Freymueller, J., N. E. King, and P. Segall (1994). The co-seismic slip distribution of the Landers earthquake, *Bull. Seism. Soc. Am.* **84,** 646–659.

Gordon, D., C. Ma, and J. W. Ryan (1993). Results from the CDP mobile VLBI program in the western United States, in *Contributions of Space Geodesy to Geodynamics: Crustal Dynamics, Geodynamics 23,* D. E. Smith and D. L. Turcotte (Editors), American Geophysical Union, Washington, D.C., 131–138.

Harris, R. A. and R. W. Simpson (2002). The 1999 M_w 7.1 Hector Mine, California, earthquake: a test of the stress shadow hypothesis?, *Bull. Seism. Soc. Am.* **92,** 1497–1512 (this issue).

Hauksson, E., K. Hafner, J. Hardebeck, T. Heaton, K. Hutton, H. Kanamori, P. Maechling, R. Busby, L. Zhu, J. Polet, L. M. Jones, D. Given, and D. Wald (1999). Overview of the 10/16/1999 M_w 7.1 Hector Mine, California earthquake sequence (abstract), AGU Fall 1999 Meet. Program: Late Breaking Sessions, 15.

Hauksson, E., L. M. Jones, K. Hutton, and D. Eberhart-Phillips (1993). The 1992 Landers earthquake sequence: seismological observations, *J. Geophys. Res.* **98,** 19,835–19,858.

Hibbit, Karlsson & Sorensen, Inc. (1998). ABAQUS, version 5.8, Hibbit, Karlsson & Sorensen, Inc., Pawtucket, Rhode Island.

Hudnut, K. W., Y. Bock, M. Cline, P. Fang, Y. Feng, J. Freymueller, X. Ge, W. K. Gross, D. Jackson, M. Kim, N. E. King, J. Langbein, S. C. Larsen, M. Lisowski, Z.-K. Shen, J. Svarc, and J. Zhang (1994). Co-seismic displacements of the 1992 Landers earthquake sequence, *Bull. Seism. Soc. Am.* **84,** 625–645.

Hurst, K. J., D. F. Argus, A. Donnellan, M. B. Heflin, D. C. Jefferson, G. A. Lyzenga, J. W. Parker, M. Smith, F. H. Webb, and J. F. Zumberge (2000). The coseismic geodetic signature of the 1999 Hector Mine earthquake, *Geophys. Res. Lett.* **27,** 2733–2736.

Jaeger, J. C. (1969). *Elasticity, Fracture and Fluid-flow,* Methuen and Company, London, 268 pp.

Johnson, A. M., R. W. Fleming, K. M. Cruikshank, S. Y. Martosudarmo,

N. A. Johnson, K. M. Johnson, and W. Wei (1997). Analecta of structures formed during the 28 June 1992 Landers–Big Bear, California earthquake sequence, *U.S. Geol. Surv. Open File Rept.* 97-94, 59 pp.

Johnson, H. O., D. C. Agnew, and K. Hudnut (1994). Extremal bounds on earthquake movement from geodetic data: applications to the Landers earthquake, *Bull. Seism. Soc. Am.* **84,** 660–667.

Johnston, M. J. S., A. T. Linde, and D. C. Agnew (1994). Continuous borehole strain in the San Andreas fault zone, before, during, and after the 28 June 1992, M_w 7.3 Landers, California, earthquake, *Bull. Seism. Soc. Am.* **84,** 799–805.

Jones, L. E., and S. E. Hough (1995). Analysis of broadband records from the 28 June 1992 Big Bear earthquake: evidence of a multiple-event source, *Bull. Seism. Soc. Am.* **85,** 688–704.

Kaufman, P. S., and L. H. Royden (1994). Lower crustal flow in an extensional setting: constraints from the Halloran Hills region, eastern Mojave Desert, California, *J. Geophys. Res.* **99,** 15,723–15,739.

King, G. C., R. S. Stein, and J. Lin (1994). Static stress changes and the triggering of earthquakes, *Bull. Seism. Soc. Am.* **84,** 935–953.

Kohlstedt, D. L., B. Evans, and S. J. Mackwell (1995). Strength of the lithosphere: constraints imposed by laboratory experiments, *J. Geophys. Res.* **93,** 17,587–17,602.

Madsen, S. N., and H. A. Zebker (1998). Imaging radar interferometry, in *Principles and Applications of Imaging Radar,* F. M. Henderson and A. J. Lewis (Editors) John Wiley & Sons, New York, 359–380.

Massonnet, D., M. Rossi, C. Carmona, F. Adragna, G. Peltzer, K. Feigl, and T. Rabaute (1993). The displacement field of the Landers earthquake mapped by radar interferometry, *Nature* **364,** 138–142.

Massonnet, D., W. Thatcher, and H. Vadon (1996). Detection of postseismic fault zone collapse following the Landers earthquake, *Nature* **382,** 612–616.

Masterlark, T. L. (2000) Regional fault mechanics following the 1992 Landers earthquake, *Ph.D. Thesis,* University of Wisconsin–Madison, Madison, Wisconsin, 83 pp.

Masterlark, T. L., and H. F. Wang, Poroelastic coupling between the 1992 Landers and Big Bear earthquakes, *Geophys. Res. Lett.* **27,** 3647–3650.

Masterlark, T., C. DeMets, H. F. Wang, J. Stock, and O. Sanchez (2001) Homogeneous vs. realistic heterogeneous material properties in subduction zone models: coseismic and postseismic deformation, *Geophys. Res. Lett.* **28,** 4047–4050.

Masterlark, T., H. Wang, L. Chan, and Y. Che (1999). Coseismic fluidpressure response estimated from prediction-error filtering of tidalband loading, *Bull. Seism. Soc. Am.* **89,** 1439–1446.

Miller, M. M., D. J. Johnson, T. H. Dixon, and R. K. Dokka (2001). Refined kinematics of the eastern California shear zone from GPS observations, 1993–1998, *J. Geophys. Res* **106,** 2245–2263.

Murray, M. H., J. C. Savage, M. Lisowski, and W. K. Gross (1993). Coseismic displacements: 1992 Landers, California, earthquake, *Geophys. Res. Lett.* **20,** 623–626.

Okada, Y. (1992). Internal deformation due to shear and tensile faults in a half-space, *Bull. Seism. Soc. Am.* **82,** 1018–1040.

Parsons, T., and D. S. Dreger (2000) Static-stress impact of the 1992 Landers earthquake sequence on nucleation and slip at the site of the 1999 $M = 7.1$ Hector Mine earthquake, southern California, *Geophys. Res. Lett.* **27,** 1949–1952.

Peltzer, G., P. Rosen, F. Rogez, and K. Hudnut (1996). Postseismic rebound in fault step-overs caused by pore fluid-flow, *Science* **273,** 1202–1204.

Peltzer, G., P. Rosen, F. Rogez, and K. Hudnut (1998). Postseismic rebound along the Landers 1992 earthquake surface rupture, *J. Geophys. Res.* **103,** 30,131–30,145.

Pollitz, F. F. (1997). Gravitational viscoelastic postseismic relaxation on a layered spherical earth, *J. Geophys. Res.* **102,** 17,921–17,941.

Pollitz, F. F., R. Bürgmann, and P. Segall (1998). Joint estimation of afterslip rate and postseismic relaxation following the 1989 Loma Prieta earthquake, *J. Geophys. Res.* **103,** 26,975–26,992.

Pollitz, F. F., G. Peltzer, and R. Bürgmann (2000). Mobility of continental

mantle: evidence from postseismic geodetic observations following the 1992 Landers earthquake, *J. Geophys. Res.* **105,** 8035–8054.

Qu, J., T. L. Teng, and J. Wang (1994). Modeling of short-period surface-wave propagation in southern California, *Bull. Seism. Soc. Am.* **84,** 596–612.

Roeloffs, E. A. (1995). Poroelastic techniques in the study of earthquake-related hydrologic phenomena, *Adv. Geophys.* **37,** 135–195.

Roeloffs, E. A., W. R. Danskin, C. D. Farrar, D. L. Galloway, S. N. Hamlin, E. G. Quilty, H. M. Quinn, D. H. Schaefer, M. L. Sorey, and D. E. Woodcock (1995). Hydrologic effects associated with the June 28, 1992 Landers, California, earthquake sequence, *U.S. Geol. Surv.* Open-File Rept. 95-42.

Sandwell, D. T., L. Sichoix, D. Agnew, Y. Bock, and J.-B. Minster (2000). Near real-time radar interferometry of the M_w 7.1 Hector Mine earthquake, *Geophys. Res. Lett.* **27,** 3101–3104.

Savage, J. C. (1990). Equivalent strike-slip earthquake cycles in half-space and lithosphere–asthenosphere Earth models, *J. Geophys. Res.* **95,** 4873–4879.

Savage, J. C., and J. L. Svarc (1997) Postseismic deformation associated with the M_w 7.3 1992 Landers earthquake southern California, *J. Geophys. Res.* **102,** 7565–7577.

Scientists of the U.S. Geological Survey, Southern California Earthquake Center, and California Division of Mines and Geology (2000). Preliminary report on the 10/16/1999 M7.1 Hector Mine, California earthquake, *Seism. Res. Lett.* **71,** 11–23.

Shen, Z. K., D. D. Jackson, Y. Feng, M. Cline, M. Kim, P. Feng, and Y. Bock (1994). Postseismic deformation following the Landers earthquake, California, 28 June 1992, *Bull. Seism. Soc. Am.* **84,** 780–791.

Toda, S., R. Stein, and G. King (2001). Coulomb 2.0. Published by Earthquake and Volcano Deformation and Stress Triggering Research Group, USGS Earthquake Hazards Program, Menlo Park, CA. Software can

be downloaded from http://quake.usgs.gov/research/deformation/ modeling/coulomb/coulomb20/software.html

Turcotte, D. L., and G. J. Schubert (1982). *Geodynamics: Applications of Continuum Physics to Geological Problems,* John Wiley & Sons, New York, 450 pp.

Wald, D. J., and T. H. Heaton (1994). Spatial and temporal distribution of slip for the 1992 Landers, California, earthquake, *Bull. Seism. Soc. Am.* **84,** 668–691.

Wang, H. F. (2000) *Theory of Linear Poroelasticity: With Applications to Geomechanics,* Princeton Univ. Press, Princeton, New Jersey, 287 pp.

Wyatt, F. K., D. C. Agnew, and M. Gladwin (1994). Continuous measurements of crustal deformation for the 1992 Landers earthquake sequence, *Bull. Seism. Soc. Am.* **84,** 768–779.

Wyss, M., and S. Wiemer (2000). Change in the probability for earthquakes in southern California due to the Landers magnitude 7.3 earthquake, *Science* **290,** 1334–1338.

Wyss, M., S. Hreinsdóttir, and D. A. Marriott (1999). Southern extent of the October 1999 M_w 7.1 Hector Mine earthquake limited by Coulomb stress changes due to the M7.3 Landers earthquake of 1992 (abstract), AGU Fall 1999 Meet. Program: Late Breaking Sessions, 16–17.

U.S. Geological Survey
EROS Data Center, Raytheon
Sioux Falls, South Dakota 57198
   (T.M.)

Department of Geology and Geophysics
University of Wisconsin–Madison
Madison, Wisconsin 53706
   (H.F.W.)